Interpretable Geoscience Artificial Intelligence (XGeoS-AI): Application to Demystify Image Recognition

Jin-Jian Xu[1], Hao Zhang[2], Chao-Sheng Tang[3]*, Lin Li[4], Bin Shi[5]

1. School of Earth Sciences and Engineering, Nanjing University, 163 Xianlin Road, Nanjing 210023, China. E-mail: Xujianjian@smail.nju.edu.cn.

2. College of Electronic and Information Engineering, Nanjing University of Aeronautics and Astronautics, Nanjing 210016, China. Email: haozhangcn@nuaa.edu.cn.

3. School of Earth Sciences and Engineering, Nanjing University, 163 Xianlin Road, Nanjing 210023, China. E-mail: tangchaosheng@nju.edu.cn.

4. School of Earth Sciences and Engineering, Nanjing University, 163 Xianlin Road, Nanjing 210023, China. E-mail: linli@smail.nju.edu.cn.

5. School of Earth Sciences and Engineering, Nanjing University, 163 Xianlin Road, Nanjing 210023, China. E-mail: shibin@nju.edu.cn.

Jin-Jian Xu and Hao Zhang contributed equally to this work.

Corresponding author*:

Chao-Sheng Tang, E-mail: tangchaosheng@nju.edu.cn

Abstract

As Earth science enters the era of big data, artificial intelligence (AI) not only offers great potential for solving geoscience problems, but also plays a critical role in accelerating the understanding of the complex, interactive, and multiscale processes of Earth's behavior. As geoscience AI models are progressively utilized for significant predictions in crucial situations, geoscience researchers are increasingly demanding their interpretability and versatility. This study proposes an interpretable geoscience artificial intelligence (XGeoS-AI) framework to unravel the mystery of image recognition in the Earth sciences, and its effectiveness and versatility is demonstrated by taking computed tomography (CT) image recognition as an example. Inspired by the mechanism of human vision, the proposed XGeoS-AI framework generates a threshold value from a local region within the whole image to complete the recognition. Different kinds of artificial intelligence (AI) methods, such as Support Vector Regression (SVR), Multilayer Perceptron (MLP), Convolutional Neural Network (CNN), can be adopted as the AI engines of the proposed XGeoS-AI framework to efficiently complete geoscience image recognition tasks. Experimental results demonstrate that the effectiveness, versatility, and heuristics of the proposed framework have great potential in solving geoscience image recognition problems. Interpretable AI should receive more and more attention in the field of the Earth sciences, which is the key to promoting more rational and wider applications of AI in the field of Earth sciences. In addition, the proposed interpretable framework may be the forerunner of technological innovation in the Earth sciences.

Keywords: Earth science, Artificial intelligence, Interpretable framework, Human vision, AI engines

1 Introduction

Geoscience is not only a fascinating field that studies the formation, evolution, and interactions of the Earth's layers, but also a socially significant field that addresses the numerous pressing issues facing humanity and the planet (Bergen et al., 2019). Currently, we face enormous challenges associated with geosciences, such as predicting extreme climate changes, monitoring the transport of pollutants in soil, coordinating the sustainable utilization of water resources and mineral resources, revealing the causes of disasters involving earthquakes, landslides, floods, and volcanic eruptions (Bolt et al., 2013; Cosgrove and Loucks, 2015; Xie et al., 2015). The main difficulty in solving the above-mentioned issues lies in the multidisciplinary of physics, geology, hydrology, ecology, and anthropology (Karpatne et al., 2018). Meanwhile, multidisciplinary intersection inevitably leads to the complexity, multi-source, and discreteness of datasets. Geoscience datasets are often compiled from three main types of data: (i) remote sensing data acquired by Earth observation satellites; (ii) data gathered by on-site sensors from the ocean, land, or air; and (iii) simulation data based on physical models of the Earth system (Faghmous and Kumar, 2014; Karpatne et al., 2015). Geoscientists must figure out how to sift through vast volumes of data to get the most relevant information possible and how to derive new insights from data, simulations, and the links between them (Bergen et al., 2019). Unprecedented data sources, ever-increasing computing power, and recent advances in statistical modeling and machine learning provide exciting new opportunities to deepen our understanding of the Earth sciences from vast amounts of data (Reichstein et al., 2019).

With the continuous development of artificial intelligence (AI), various convolutional neural networks (CNNs) with high classification and recognition accuracy have achieved remarkable results, which have been widely used in image recognition, data mining, natural language processing (LeCun et al., 2015; Zhang and Hong, 2019). Unlike conventional model-driven approaches, AI is a data-driven approach that trains regression or classification models using complicated nonlinear mappings and configurable parameters on the basis of a training dataset (Yu and Ma, 2021). As Earth science enters the era of big data, AI not only has enormous promise for resolving geoscience-related issues, but also significantly advances our knowledge of the intricate, interacting, and multiscale processes that shape Earth's behavior (Camps-Valls et al., 2021; Irrgang et al., 2021). This revolution of the geoscience AI has been driven by the simultaneous introduction of new algorithms, the influx of large amounts of high-quality data, and the increased computing power to process large amounts of data simultaneously (Sun et al., 2022; Zhang et al., 2022).

AI models are emerging as powerful tools for scientific applications across all branches of the Earth sciences. Earth's water has a large impact on ecosystem stability and the frequency of natural disasters, and AI can help solve many challenging tasks in marine science (Shen, 2018; Malde et al., 2020). For instance, AI can not only predict ocean circulation by learning patterns of sea surface height (SSH), but also reconstruct SSH across the North-Sea using observational data from satellites and coastal stations (Zhang et al., 2020). In solid Earth science, artificial intelligence (AI) is frequently used to automate the analysis of large-scale geoscience data, including classifying volcanic ash particles to infer eruption mechanisms, as well as using remote sensing data for geological mapping and describing the topology of fracture systems (Bergen et al., 2019; Beroza et al., 2021; Rouet-Leduc et al., 2021). AI applications in atmospheric science are mainly focused on the observation and prediction of weather and climate (Huntingford et al., 2019). Global warming leads to frequent occurrence of extreme climates, seasonal weather forecasting, prediction of extreme events such as floods or fires, and long-term climate forecasting remain the main challenges for the application of AI in atmospheric science (Bauer et al., 2015; Dueben et al., 2022). AI can help to improve the accuracy of weather forecasts and extreme weather forecasts, not only reconstruct missing values in global climate datasets, but can also predict typhoon trajectories six hours in advance based on satellite imagery based on Generative Adversarial Network (GAN) (Rüttgers et al., 2019; Kadow et al., 2020; Mansfield et al., 2020). In summary, it can be found that AI is mainly used to complete the classification and prediction work in the fields of marine science, solid Earth science, and atmospheric science, especially in the recognition of geoscience images.

However, the conventional geoscience image recognition models are always heavy with a huge number of trainable parameters in an encoder-decoder way, and a parameter space may consist of hundreds of layers and millions of parameters. In addition, a mass of manually labeled geoscience images is required for the training of these heavy recognition models, which is time-consuming and labor-intensive. Finally, and most importantly, the geoscience image recognition process is still an unexplainable black box, which also greatly limits the application and promotion of the relevant AI models in the field of the Earth sciences. Therefore, it is urgent to develop a lightweight, modularized, and interpretable AI framework that can be applied to the Earth sciences, which can directly and transparently understand the working mechanism of the model and break the black box of geoscience AI.

2 Methodology

2.1 Interpretable Geoscience Artificial Intelligence (XGeoS-AI) Framework

The main risk of black-box AI models is that the decisions made may be irrational, illegal, or their behavior cannot be explained in detail. The inexplicability of AI models in solving geoscience problems makes researchers hesitant to use AI. Understanding how and why models make decisions is important for rationally solving crucial geoscience problems. As shown in Fig 1, the conventional geoscience artificial intelligence (GeoS-AI) treats the neural network as a function, where the collected training data is put into the function and trained. Then, the learned function generates an output with a probability. The user can only get a result with a probability, not understanding the process. On the contrary, the proposed interpretable geoscience artificial intelligence (XGeoS-AI) takes the learning process as a coupled model associated with the task, which can not only give the result but also the reason why the decision is made. The process of the interpretable model is transparent and can be easily understood by the user. Inspired by the process of human decision, we propose a XGeoS-AI framework for demystifying the working mechanism of geoscience image recognition.

As shown in Fig 2(a), in the procedure of human decision in classifying vision signals, it often takes two steps to make an accurate decision (Bonner and Epstein, 2021). The first step is often the process of getting visional representation from the environment, and the representation may cause spiking in the neurons. Then, high level semantic information is generated in the second step to make the decision according to the knowledge stored in the brain. For example, in the process of soil crack recognition, the first step is the process of feature learning of the crack, and then the second step in the decision process of whether the pixel belongs to crack or not. The previous works (Xu et al., 2022a) summarized the process of decision as the classification of every pixel, which is the combination of low-level vision and high-level. However, when making decision, the brain works in a high-level step, where semantic information is introduced and the spiking information is generated. Thus, in this work, we treat the second step as a human decision process, where a threshold is projected. Specifically, in the first stage, an AI engine is utilized to predict the threshold of the geoscience images, where the AI engine can be selected from most of the models in machine learning and deep learning (as presented in Fig 2(b)). Detailly, Support Vector Regression (SVR) (Drucker et al., 1997), Multilayer Perceptron (MLP) (Gardner and Dorling, 1998), and Convolutional Neural Network (CNN) (LeCun et al., 1998; Albawi et al., 2017) are demonstrated in this study. Then, in the second stage, the predicted threshold is used to generate the final output images. The whole framework is constructed with respect to the process of human decision, which makes the process interpretable. The

reason why chooses these three AI engines is that they are the most common tools in machine learning and deep learning. SVR is a representative model of machine learning, which is transferred from support vector machine (SVM). MLP is an intermedia model from the age of machine learning and deep learning, while CNN is one of the most powerful models in the era of deep learning.

2.2 AI Engines

(1) Support Vector Regression (SVR)

SVR is a variation of Support Vector Machines (SVMs) (Hearst et al., 1998) for use in regression situations, keeping all the key characteristics of the method (maximal margin). SVR seeks to fit the best line within a threshold value whereas the majority of regression models work to reduce the difference between the real value and the projected value. Consider the blue and green lines in Fig 2(c) to be the decision boundaries, and the red line to be the hyperplane. Essentially, the goal is to take into account the points that are inside the decision boundary line. The hyperplane that has covered the most points is considered to be the greatest fit line. Assuming that the hyperplane's equation is as follows

$$f(x) = wx + b \tag{1}$$

Then, the equations of decision boundary are

$$f(x) + \epsilon \tag{2}$$

$$f(x) - \epsilon \tag{3}$$

Consequently, every hyperplane satisfying the SVR should meet

$$-\epsilon < f(x) = wx + b < \epsilon \tag{4}$$

Finding a decision boundary at ϵ away from the hyperplane is the primary objective. Then, the data points or support vectors have to be as near to the hyperplane or the boundary line as possible. The lowest rate of error can be achieved only by considering data points within the decision border. Therefore, the hyperplane that touches the most data points is the optimal choice in SVR.

(2) Multilayer Perceptron (MLP)

MLP is a kind of neural network models that can approximate any continuous function. It is composed of neurons called perceptions. A perceptron takes n characteristics as input $\mathbf{x}=(x_1,x_2,\ldots,x_n)$, each of which is assigned a weight. The input characteristics are supplied to an input function u, which computes their weighted sum.

$$u(\mathbf{x}) = \sum_{i=1}^{n} w_i x_i \tag{5}$$

The output of the perceptron is created by an activation function f, which receives the outcome of this calculation. The activation function of the original perceptron is a step function.

$$y = f(u(x)) = \begin{cases} 1, & \textbf{if } u(x) > \theta \\ 0, & \textbf{otherwise} \end{cases} \tag{6}$$

where θ is a threshold parameter.

MLP is able to approximate any continuous function by combining several neurons, which are organized into at least three layers, namely, the input layer, the hidden layers, and the output layer. The input layer is used to transfer the input features to the first hidden layer. The hidden layers take in the output features from the input layer and map them into a higher dimensional space. The output layer generates the representation of the target space. Fig 2(d) shows a scheme of an MLP with two hidden layers. By mixing many neurons that are arranged in at least three layers, namely the input layer, hidden layers, and output layer, the MLP is able to approximate any continuous function. The input layer is used to transfer the input features to the first hidden layer. The hidden layers take in the output features from the input layer and map them into a higher dimensional space. The output layer generates the representation of the target space. A diagram of an MLP with two hidden layers is shown in Fig 2(d). Sigmoid functions are commonly used for the buried layer neurons. Smooth transitions rather than rigid decision boundaries, as they do when step functions are used, are produced by sigmoid functions. For classification difficulties and regression problems, the activation function of the output layer neurons is commonly sigmoid.

(3) Convolutional Neural Network (CNN)

CNNs are a subset of neural networks that are better at processing inputs that include images, voice, or audio than other neural networks. As shown in Fig 2(e), it consists of three basic types of layers: convolutional layer, pooling layer, and fully-connected (FC) layer (Gholamalinezhad and Khosravi, 2020). The fundamental component of a CNN is

the convolutional layer. Convolution, the primary process in the convolutional layer, is the computation of a feature map using a feature detector, often referred to as a kernel or a filter, and the subsequent generation of a new feature map. The feature map's size is decreased through dimensionality reduction carried out by the pooling layers, also known as down-sampling. The output feature map is produced by the pooling kernel after applying an aggregation function to the data in the receptive field. Max pooling and average pooling are the two primary forms of pooling. While average pooling determines the average value inside the input feature map to the output, max pooling chooses the pixel with the largest value as the output. Although the information is lost in the pooling layer, it also helps to minimize complexity, boost productivity, and lessen the danger of overfitting. The learned feature map from the convolutional layers is often transferred into the target space using the FC layer, which is the sole layer of the MLP (Glorot et al., 2011). This results in a probability ranging from 0 to 1.

2.3 Experiments and Evaluation Metrics

(1) Threshold Generation

When the human brain decides whether the pixel of the geoscience image is an object that needs to be focused on, a judgment threshold is actually generated in the neurons according to the spiking information. However, human brain cannot provide the threshold directly in a visual way. Thus, in order to generate the optimal judgment threshold, a simple heuristic algorithm is constructed by trying all pixel values and compare all the obtained recognition results with the ground truth of manual annotation to obtain the optimal threshold. To finish this algorithm, the pixels from 0 to 255 are used to generate the result based on the metrics below (including precision (P) and recall (R), Dice, and Jaccard) (Milletari et al., 2016). The process is very time-consuming because the loop will become ten or a hundred times to get a more precise pixel threshold. Thus, only integral value is generated in this work. The detail process of the adopted threshold generation algorithm is shown in Table 1.

(2) Implementation and Loss function

Scikit-learn (Pedregosa et al., 2011), a Python machine-learning package, is used to implement the SVR. PyTorch (Paszke et al., 2019), a Python-based deep learning package, is used to build the MLP and CNN. The mean squared error (MSE)

(Wang and Bovik, 2009), which is the most used loss function for regression, is used to assess the learning process. The difference between the actual and forecasted numbers, squared, is the loss, or you can write it as a formula.

$$L(y,\hat{y}) = \frac{1}{N}\sum_{i=0}^{N}(y-\hat{y}_i)^2 \tag{7}$$

where y is the true value and $\hat{y}$ is the predicted value.

(3) Evaluation Metrics

To evaluate the performance of the proposed interpretable framework for geoscience image recognition, different metrics are utilized. As in our earlier efforts, popular metrics like accuracy, recall, and dice coefficient are specifically utilized (Xu et al., 2022b).

$$P = \frac{TP}{TP+FP} \tag{8}$$

$$R = \frac{TP}{TP+FN} \tag{9}$$

where *TP* stands for true positive, meaning that pixels that are predicted as positive labels are actually positive labels, *FP* is for false positive, and *FN* is for false negative. Precision (*P*) and recall (*R*) calculate the quantitative relationship between the amount of correctly sorted pixels and the total number of them. The dice coefficient calculates how similar two samples are. The performance improves when the dice are rolled higher. By way of *TP*, *FP*, and *FN*, the dice coefficient may be summed up as follows

$$Dice = \frac{2\times TP}{(TP+FP)+(TP+FN)} = \frac{2|G\cap P|}{|G|+|P|} \tag{10}$$

The Jaccard index is given as a further illustration of the usefulness of the suggested framework. Similarity and variety in samples may be evaluated using the Jaccard index, often known as the Jaccard similarity coefficient, which is defined as

$$Jaccard = \frac{|G\cap P|}{|G\cup P|} = \frac{|G\cap P|}{|G|+|P|-|G\cap P|} \tag{11}$$

3 Data sets

3.1 Testing soil

The tested soil, named Pukou soil, is a typical expansive soil sampled at a depth of 0.5-1.0 m from a site in Nanjing, Jiangsu Province, China. This typical soil will be found in many important regional construction projects in the middle and downstream areas of the Yangtze River. Table 2 lists the physical properties of the tested soils. In accordance with the Unified Soil Classification System (ASTM D-2487, 2017), the Pukou soil can be categorized as a high plasticity clay (CH). It is noted that Pukou soil has 24%, 34% and 42% of sand, silt and clay, respectively. The clay fraction is dominated by montmorillonite.

3.2 Data collection

The retrieved natural soil was dried and pulverized in turn, and sieved through a 2 mm sieve. Then add an appropriate amount of water to the pulverized soil and stir well to control its initial water content to 25.0%. The prepared soil was put into a sealed bag and placed for 48 hr to make the water distribution uniform. The moist soil of the required quality for specimen preparation was equally divided into four parts and poured into a stainless-steel mold with a diameter of 50 mm for static compaction, and each soil layer was compacted to the same thickness of 25 mm. The height and diameter of the soil specimen were 100 mm and 50 mm, respectively, and the initial dry density was compacted to 1.3 Mg/m^3. As shown in Fig 3(a), the soil specimen was then placed in a saturation device for seven days under confined conditions. Filter papers and porous stones were placed on the top and bottom, which not only provide reliable support, also allow free entry and exit of liquid and gas. In addition, the saturation device is connected to a vacuum pump to expedite and confirm that the soil specimen is completely saturated. Subsequently, the saturated soil specimen with an initial water content of approximately 42.5% were placed at a steady temperature of 30°C during the drying test. According to the development of cracks during the drying process, the soil specimens with different water contents of 42.5%, 37.3%, 36.4%, 34.1%, 29.2%, 25.0%, and 15.6% were used to conduct X-ray computed tomography (X-CT) scanning tests and obtain the CT images of internal cracks (as displayed in Fig 3(b-c)).

X-CT is an effective technique that allows non-destructive observation of the internal structure of an object (Gouze et al., 2003). The technique is capable of capturing the difference in object density by emitting X-rays that perforate the target object from numerous directions (Cnudde & Boone, 2013). The apparatus used in the CT scanning test was an X-

CT scanner (Somatom Sensation 40, produced by Siemens Corporation, Germany) from the Yangtze River Scientific Research Institute of China. During the scanning test, the X-ray source of the apparatus was tilted ±30° and moved along a circle with a diameter of 70 cm at a rotational speed of 0.37 s per cycle. The X-ray source will emit X-rays towards the soil specimen that placed in the center of the circle and the attenuated X-rays will be collected by a detector opposite the source. The X-ray generator power of the apparatus was 70 kW and the tube voltage was 140 kV, and the scanner resolution was 0.06 mm/pixel. By means of X-CT scanning technique, 46 2D slice images of the middle horizontal section of soil specimens were obtained, and each 2D slice had a thickness of 0.06 mm, contained 336 × 336 pixels, and a pixel size of 0.147 × 0.147 mm. For model training, soil crack CT image dataset contains 40 2D slice images with a size of 336 × 336 pixels. The remaining 6 2D slice images with the same size are used for model testing. As presented in Fig 3(d), all 2D slice images are human-annotated with the ground truth using Labelme (a Python-written visual picture annotation tool). The areas of soil cracks are marked using a red polygon line, and the red area is the ground truth of the crack.

4 Results and Discussion

4.1 Visualization of the recognition results

To demonstrate the effectiveness of the proposed XGeoS-AI framework for geoscience image recognition, both numerous and visual results are presented in this section. The label of T1-T5 stands for the selected five test images. As shown in Fig 4, we visualize the recognition results of all the test images (T1-T5) and compare the ability of threshold prediction of the framework empowered by different kinds of AI engines. The “TRUE” is the recognition result obtained by the above simple heuristic algorithm, which will be compared with the result obtained by using the different AI engines (SVR, MLP, CNN). On the whole, the proposed framework uses different AI engines can effectively recognize the target (crack) of CT images. The recognition effect of T1, T2, T5, and T6 can basically be parallel to the “Ture” (similar to human visual recognition). It can be found that, for images with multiple noisy spots such as T3 and T4, the proposed framework cannot perform very well, especially for the MLP which uses a simple architecture. Although the recognition effects of T3 and T4 are not prominent and there are many miscellaneous spots in recognition images, the soil cracking recognition is still relatively accurate. The main reason for this phenomenon may be that the existence of these spots will influence the prediction of the recognition threshold. In addition, the AI engine used in the proposed framework to

recognize the target (crack) of CT images is the most basic machine learning (ML) algorithm. However, these independent spots are easy to be overcome, which can be eliminated by using tools such as random conditional field in our previous work (Xu et al., 2022a). Otherwise, denoising can be operated before the process of recognition to remove these spots. Moreover, more powerful AI engines such as deeper CNNs or other models can be utilized with our proposed framework to achieve a better performance to get rid of the influence of these spots (Xu et al., 2022b). If you want to achieve better results, geoscience researchers can use more advanced ML algorithms such as UNet, Res-UNet, Attention Res-UNet, and so on (Xu et al., 2022a, 2022b). Thus, in spite of these special situations such as multiple noise spots, the proposed interpretable AI framework can work very well with quite simple AI engines such as SVR, MLP, and CNN.

4.2 Quantitative analysis of the recognition performances

To further demonstrate the effectiveness of the proposed XGeoS-AI framework, the numerous performance comparison of different AI engines (SVR, MLP, CNN) with the proposed framework is illustrated in Fig 5. Notice that the label "TRUE" stands for the results generated using the optimal threshold from the simple heuristic algorithm, which is taken as the standard. Under these criterions, these AI engines with the proposed framework can obtain comparable performance with the standard performance. As shown in Fig (a), the optimal thresholds obtained by different AI engines are similar to the "TRUE" (similar to human visual recognition). Subsequently, the overall performance in terms of precision, recall, dice and Jaccard is evaluated and presented in Fig 5(b), our proposed framework exceeds the standard method in terms of recall, which means that the framework can recognize the crack more accurately. To evaluate the performance of the proposed framework more detailly, we give the numerous results of dice and Jaccard on every test image in Fig 5(c-d). It can be observed that the proposed framework can acquire almost the same performance compared to the standard method (simple heuristic algorithm) except for T3 and T4. Nevertheless, the emergence of T3 and T4 recognition problems has been detailly discussed in the visual results. In summary, the proposed XGeoS-AI framework can not only performance very well in terms of both numerous and visual performance. Most importantly, the process of the XGeoS-AI framework is interpretable, while not a black box as the previous recognition models. Interpretable also means that we understand its process and the decisions made, which also makes our proposed framework easier for geoscience researchers to trust.

5 Implications and Further Discussion

The successful application of AI in geoscience stems from the combination of efficient machine learning algorithms and their enormous parameter spaces, which may consist of hundreds of layers and millions of parameters. Therefore, the AI model has always been regarded as a complex black-box model. As AI models in the geoscience field are increasingly used to generate significant predictions in challenging conditions, geoscience researchers are increasingly demanding their transparency. The risk of black-box AI models is that the decisions made and used may be irrational, illegal, or their behavior cannot be explained in detail. The inexplicability of AI for geoscience science has made researchers hesitant to use it because understanding how and why models make decisions is important for rationally solving scientific problems. Therefore, in order to promote the application of AI in the field of the Earth sciences, the interpretable geoscience AI proposed in this study is essential and necessary.

For the decision-making habits of geoscience researchers, the explanation for AI must be non-trivial, non-artificial, and provide sufficient information for the geoscience community. Interpretability requires considering the trade-off between accuracy and fidelity, and finding a balance between accuracy, interpretability, and tractability. Therefore, interpretable AI, as a means of explaining inherently unexplainable machine black-box models and deep learning, should receive more and more attention in the Earth sciences, which is to promote more rational and wider application of AI in the Earth sciences. This is the significance view that needs to be clarified and highlighted in this study.

Understanding and interpreting classification decisions for image semantic segmentation is of high value in many geoscience applications, as it can justify the decision-making process and provide geoscience researchers with additional information. For example, although we have used AI to recognize complex soil cracks, so as to obtain more information about the development pattern of soil crack networks in a more accurate and fair way, which also provides support and guarantee for our further research on the formation mechanism of soil cracking. However, the AI models used in previous studies are uninterpretable, we only know the input original image, and then get the recognition result we want. It is unknown how the entire recognition process is carried out, which is also the concern of many geoscience researchers. The XGeoS-AI framework proposed in this study can dispel the concern. We visualize the entire recognition process of soil cracks by combining the process of human visual decision-making, thus achieving the interpretability of the AI model, which also demonstrates the effectiveness of the proposed framework through soil cracks recognition.

In order to verify the versatility of the proposed XGeoS-AI framework for solving other geoscience image recognition problems, we randomly selected ten granite CT images and obtained the biotite distribution of the granites, seven of granite CT images were used for model training and three for model testing. As illustrated in Fig 6(a), we utilize the proposed framework together with three AI engines (SVR, MLP, CNN) for training and testing on the granite CT dataset. The recognition of biotite distribution by the proposed framework is shown in Fig 6(b). The visualization results show that the XGeoS-AI framework can accurately obtain the biotite distribution in granite CT images using three AI engines, and the numerous performances of the four evaluation metrices (precision, recall, dice and Jaccard) in biotite distribution recognition are all greater than 0.96 (displayed in Table 3). This not only proves once again the effectiveness and interpretability of the proposed XGeoS-AI framework in recognizing geoscience images, but also clarifies its versatility in solving geoscience image recognition problems. Last but not the least, the XGeoS-AI framework can not only be applied for image recognition, but also can be used in many other areas of the Earth sciences, such as prediction, classification.

The interpretability of the machine learning model especially the deep learning model is hard to be evaluated. Thus, we adopt a Shapley Additive Explanations (SHAP) approach to assess the interpretability of the proposed framework for geoscience image recognition (Štrumbelj and Kononenko, 2014). SVM has a rigorous mathematical derivation, so the interpretability of SVM is natural, which is no need for further demonstration. Thus, we only analyze the deep models MLP and CNN for the engines in our proposed XGeoS-AI framework, as shown in Fig 7. The first and second columns show the test images and corresponding masks as the reference for the later SHAP values, and the third and fourth columns give the visualized SHAP values of CNN and MLP, respectively. It can be found that the SHAP values of the CNN engine are not very large, while it can still indicate the region where the biotite is. On the contrary, the SHAP values of the MLP engine are distinct, and the higher values (labeled in red) indicate the biotite region. The visualization of the SHAP values of these two engines further demonstrates the interpretability of the proposed XGeoS-AI framework, in which the decision process of these engines becomes explainable by using the XGeoS-AI framework though they have no natural interpretability.

6 Conclusions

In this study, XGeoS-AI framework is proposed to unravel the mystery of image recognition in the Earth sciences, and its effectiveness and versatility is demonstrated by taking CT image recognition as an example. The effectiveness, versatility and heuristics of the proposed XGeoS-AI framework have great potential in solving geoscience image recognition problems. Major conclusions are drawn as following:

(1) Inspired by the mechanism of human vision, the XGeoS-AI framework is proposed by using the idea of local threshold and artificial intelligent engines. Various models can be applied in the proposed XGeoS-AI framework as AI engines to generate the local threshold in a human decision level.

(2) Three distinct types of AI engines analyze the geoscience images to determine the efficacy of the suggested framework. The experimental results demonstrate the effectiveness of the elegant XGeoS-AI framework, where the results of three different AI engines can perform as better as the true value. Moreover, the application of these engines has demonstrated the universal ability of the proposed framework, and others models can also be applied in the framework.

(3) The effectiveness, versatility and heuristics of the XGeoS-AI framework have great potential in solving geoscience image recognition problems. Thus, the XGeoS-AI framework should receive more and more attention in the field of the Earth sciences, which is the key to promoting more rational and wider applications of AI in the field of the Earth sciences. This is mainly because that XGeoS-AI can make the conventional GeoS-AI more interpretable and universal, which means that the decision process will become more transparent and reliable. For GeoS-AI, interpretable, transparent, and reliable are as important as its high performance. Therefore, XGeoS-AI may be a better choice for the field of the Earth sciences.

Acknowledgments

This work was supported by the National Natural Science Foundation of China (Grant No. 41925012, 42230710 42172290), Natural Science Foundation of Jiangsu Province (Grant No. BK20211087), China Scholarship Council (Grant No. 202206190069), Key Laboratory Cooperation Special Project of Western Cross Team of Western Light, CAS (Grant No. xbzg-zdsys-202107), and the Fundamental Research Funds for the Central Universities.

CRediT authorship contribution statement

Jin-Jian Xu: Formal analysis, Investigation, Methodology, Writing – original draft. Hao Zhang: Investigation, Methodology, Writing – original draft. Niklas Boers: Methodology, Writing – review & editing. Lin Li: Investigation, Visualization. Chao-Sheng Tang: Conceptualization, Funding acquisition, Methodology, Writing – review & editing, Project administration, Supervision.

Data Availability Statement

All data in this study are available online (https://doi.org/10.5281/zenodo.7353297).

References

Albawi, S., T. A. Mohammed, and S. Al-Zawi (2017), Understanding of a convolutional neural network, *2017 International Conference on Engineering and Technology (ICET)*, IEEE, New York, pp 1-6.

Bauer, P., A. Thorpe, and G. Brunet (2015), The quiet revolution of numerical weather prediction, *Nature*, 525(7567), 47-55.

Bergen, K. J., P. A. Johnson, M. V. de Hoop, and G. C. Beroza (2019), Machine learning for data-driven discovery in solid Earth geoscience, *Science*, 363(6433), 1299-+.

Beroza, G. C., M. Segou, and S. M. Mousavi (2021), Machine learning and earthquake forecasting-next steps, *Nat. Commun.*, 12(1), 1-3.

Bonner, M. F., and R. A. Epstein (2021), Object representations in the human brain reflect the co-occurrence statistics of vision and language, *Nat. Commun.*, 12(1), 1-16.

Bolt, B. A., Horn, W. L., MacDonald, G. A., and Scott, R. F (2013). Geological Hazards: Earthquakes-tsunamis-volcanoes-avalanches-landslides-floods. *Springer Science & Business Media*.

Camps-Valls, G., Tuia, D., Zhu, X. X., and Reichstein, M (Eds.) (2021). Deep learning for the Earth Sciences: A comprehensive approach to remote sensing, climate science and geosciences. *John Wiley & Sons*.

Cnudde, V., and M. N. Boone (2013), High-resolution X-ray computed tomography in geosciences: A review of the current technology and applications, *Earth Sci. Rev.*, 123, 1-17.

Cosgrove, W. J., and D. P. Loucks (2015), Water management: Current and future challenges and research directions, *Water Resour. Res.*, 51(6), 4823-4839.

Drucker, H., C. J. C. Burges, L. Kaufman, A. Smola, and V. Vapnik (1997), Support vector regression machines, *Adv Neur In*, 9, 155-161.

Dueben, P. D., Schultz, M. G., Chantry, M., Gagne, D. J., Hall, D. M. and McGovern, A (2022). Challenges and benchmark datasets for machine learning in the atmospheric sciences: Definition, status, and outlook. *Artif. Intell. Earth Syst.*, 1(3), e210002.

Faghmous, J. H., and V. Kumar (2014), A big data guide to understanding climate change: The case for theory-guided data science, *Big Data*, 2(3), 155-163.

Gardner, M. W., and S. R. Dorling (1998), Artificial neural networks (the multilayer perceptron) - A review of applications in the atmospheric sciences, *Atmos. Environ.*, 32(14-15), 2627-2636.

Gholamalinezhad, H., and Khosravi, H (2020) Pooling methods in deep neural networks, a review. arXiv preprint arXiv:2009.07485.

Glorot, X., Bordes, A., and Bengio, Y (2011) Deep sparse rectifier neural networks. *Inproceedings of the fourteenth international conference on artificial intelligence and statistics* (éd. Gordon, G., Dunson, D. and Dudık, M.) 15 (PMLR, 2011), 315-323.

Gouze, P., C. Noiriel, C. Bruderer, D. Loggia, and R. Leprovost (2003), X-ray tomography characterization of fracture surfaces during dissolution, *Geophys. Res. Lett.*, 30(5).

Hearst, M. A. (1998), Support vector machines, *IEEE Intell Syst App*, 13(4), 18-21.

Huntingford, C., E. S. Jeffers, M. B. Bonsall, H. M. Christensen, T. Lees, and H. Yang (2019), Machine learning and artificial intelligence to aid climate change research and preparedness, *Environ. Res. Lett.*, 14(12).

Irrgang, C., N. Boers, M. Sonnewald, E. A. Barnes, C. Kadow, J. Staneva, and J. Saynisch-Wagner (2021), Towards neural Earth system modelling by integrating artificial intelligence in Earth system science, *Nat. Mach. Intell.*, 3(8), 667-674.

Kadow, C., D. M. Hall, and U. Ulbrich (2020), Artificial intelligence reconstructs missing climate information, *Nat. Geosci.*, 13(6), 408-+.

Karpatne, A., and S. Liess (2015), A guide to earth science data: Summary and research challenges, *Comput. Sci. Eng.*, 17(6), 14-18.

Karpatne, A., I. Ebert-Uphoff, S. Ravela, H. A. Babaie, and V. Kumar (2019), Machine learning for the geosciences: Challenges and opportunities, *IEEE Trans. Knowl. Data Eng.*, 31(8), 1544-1554.

LeCun, Y., Y. Bengio, and G. Hinton (2015), Deep learning, *Nature*, 521(7553), 436-444.

Lecun, Y., L. Bottou, Y. Bengio, and P. Haffner (1998), Gradient-based learning applied to document recognition, *Proc. IEEE*, 86(11), 2278-2324.

Malde, K., N. O. Handegard, L. Eikvil, and A. B. Salberg (2020), Machine intelligence and the data-driven future of marine science, *ICES J. Mar. Sci.*, 77(4), 1274-1285.

Mansfield, L. A., P. J. Nowack, M. Kasoar, R. G. Everitt, W. J. Collins, and A. Voulgarakis (2020), Predicting global patterns of long-term climate change from short-term simulations using machine learning, *npj Clim. Atmos. Sci.*, 3(1).

Milletari, F., N. Navab, and S. A. Ahmadi (2016), V-net: Fully convolutional neural networks for volumetric medical image segmentation, *Int Conf 3d Vision*, 565-571.

Paszke, A., et al. (2019) Pytorch: An imperative style, high-performance deep learning library. *Advances in Neural Information Processing Systems* 32.

Pedregosa, F., et al. (2011), Scikit-learn: Machine learning in Python, *J Mach Learn Res*, 12, 2825-2830.

Reichstein, M., G. Camps-Valls, B. Stevens, M. Jung, J. Denzler, N. Carvalhais, and Prabhat (2019), Deep learning and process understanding for data-driven Earth system science, *Nature*, 566(7743), 195-204.

Rouet-Leduc, B., R. Jolivet, M. Dalaison, P. A. Johnson, and C. Hulbert (2021), Autonomous extraction of millimeter-scale deformation in InSAR time series using deep learning, *Nat. Commun.*, 12(1).

Ruttgers, M., S. Lee, S. Jeon, and D. You (2019), Prediction of a typhoon track using a generative adversarial network and satellite images, *Sci. Rep.*, 9.

Shen, C. P. (2018), A transdisciplinary review of deep learning research and its relevance for water resources scientists, *Water Resour. Res.*, 54(11), 8558-8593.

Štrumbelj, E., and Kononenko, I. (2014), Explaining prediction models and individual predictions with feature contributions. *Knowl. Inf. Syst.*, 41, 647-665.

Sun, Z. H., et al. (2022), A review of earth artificial intelligence, *Comput. Geosci.*, 159.

Wang, Z., and A. C. Bovik (2009), Mean squared error: Love it or leave it? A new look at signal fidelity measures, *IEEE Signal Process Mag.*, 26(1), 98-117.

Xie, S. P., et al. (2015), Towards predictive understanding of regional climate change, *Nat. Clim. Change*, 5(10), 921-930.

Xu, J. J., H. Zhang, C. S. Tang, Q. Cheng, B. Liu, and B. Shi (2022a), Automatic soil desiccation crack recognition using deep learning, *Geotechnique*, 72(4), 337-349.

Xu, J. J., H. Zhang, C. S. Tang, Q. Cheng, B. G. Tian, B. Liu, and B. Shi (2022b), Automatic soil crack recognition under uneven illumination condition with the application of artificial intelligence, *Eng. Geol.*, 296.

Yu, S. W., and J. W. Ma (2021), Deep Learning for Geophysics: Current and Future Trends, *Rev. Geophys.*, 59(3).

Zhang, H., and X. G. Hong (2019), Recent progresses on object detection: a brief review, *Multimed Tools Appl*, 78(19), 27809-27847.

Zhang, W. A., X. Gu, L. B. Tang, Y. P. Yin, D. S. Liu, and Y. M. Zhang (2022), Application of machine learning, deep learning and optimization algorithms in geoengineering and geoscience: Comprehensive review and future challenge, *Gondwana Res.*, 109, 1-17.

Zhang, Z. G., E. V. Stanev, and S. Grayek (2020), Reconstruction of the basin-wide sea-level variability in the north sea using coastal data and generative adversarial networks, *J Geophys Res-Oceans*, 125(12).

Table captions:

Table 1. The detail process of the adopted threshold generation algorithm.

Table 2. Basic physical properties of the Pukou soil.

Table 3. The numerous performances of the proposed XGeoS-AI framework in the biotite distribution recognition.

Table 1. The detail process of the adopted threshold generation algorithm.

Algorithm 1. Simple heuristic algorithm generates a mask using a specific threshold and find the best threshold based on the metric (mainly dice) compared to human labeled result.
Input: A crack image img with the corresponding manual label label. Output: best threshold thres. 1: for i=1 to 255 do 2: mask=img>i 3: p, r, dice, jaccard=Calculate (mask, label) 4: dice_max = dice if dice > dice_max 5: i_best = i if dice > dice_max 5: end for 6: thres=i_best

Table 2. Basic physical properties of the Pukou soil.

Soil properties	Values
Specific gravity	2.71
Liquid limit (%)	76.4
Plastic limit (%)	29.1
Plasticity index (%)	47.3
USCS classification	CH
Optimum moisture content (%)	18.3
Maximum dry density (g/cm^3)	1.69
Grain size analysis	
Sand (%)	24
Silt (%)	34
Clay (%)	42

Table 3. The numerous performances of the proposed XGeoS-AI framework in the biotite distribution recognition.

Image	TRUE				SVR				MLP				CNN			
number	P	R	D	J	P	R	D	J	P	R	D	J	P	R	D	J
Image1	0.9979	0.9866	0.9922	0.9845	0.9866	0.9979	0.9922	0.9845	0.9881	0.9930	0.9905	0.9812	0.9896	0.9741	0.9818	0.9642
Image2	0.9984	0.9872	0.9927	0.9856	0.9872	0.9984	0.9927	0.9856	0.9885	0.9945	0.9915	0.9832	0.9899	0.9756	0.9827	0.9660
Image3	0.9984	0.9879	0.9931	0.9863	0.9880	0.9982	0.9931	0.9862	0.9891	0.9938	0.9915	0.9831	0.9904	0.9727	0.9815	0.9636

Note: SVR, Support Vector Regression; MLP, Multilayer Perceptron; CNN, Convolutional Neural Network; P, Precision; R, Recall; D, Dice; J, Jaccard.

Figure captions:

Fig 1. The comparison of conventional geoscience artificial intelligence (GeoS-AI) and interpretable geoscience artificial intelligence (XGeoS-AI).

Fig 2. Interpretable geoscience artificial intelligence (XGeoS-AI) framework. (a) human-vison mechanism; (b) XGeoS-AI framework; (c)-(d) are the three typical AI engines, (c) support vector regression (SVR), (d) multilayer perceptron (MLP), (e) convolutional neural network (CNN).

Fig 3. The process of the data preparation. (a) Soil specimen (100 mm in height and 50 mm in diameter) is placed in a saturation device under confined conditions; (b) Soil specimens with different water contents of 42.5%, 37.3%, 36.4%, 34.1%, 29.2%, 25.0%, and 15.6%; (c) CT images with different soil cracking patterns; (d) Establishment of soil crack CT image dataset.

Fig 4. The visualization results of the AI engines with the proposed XGeoS-AI framework including test images, manual annotation, simple heuristic algorithm (TURE), SVR, MLP, CNN.

Fig 5. The numerous performance comparison of different artificial intelligence engines with the proposed XGeoS-AI framework. (a) The threshold comparison, (b) overall performance under precision, recall, dice and Jaccard, (c) dice performance, (d) Jaccard performance.

Fig 6. The proposed XGeoS-AI framework is applied in other geoscience image recognition (taking biotite distribution recognition in granite as an example). (a) The proposed framework together with three AI engines (SVR, MLP, CNN) for training and testing on the granite CT dataset; (b) Visualization results for biotite distribution recognition in granite.

Fig 7. The visualization of the SHAP values for CNN and MLP engines.

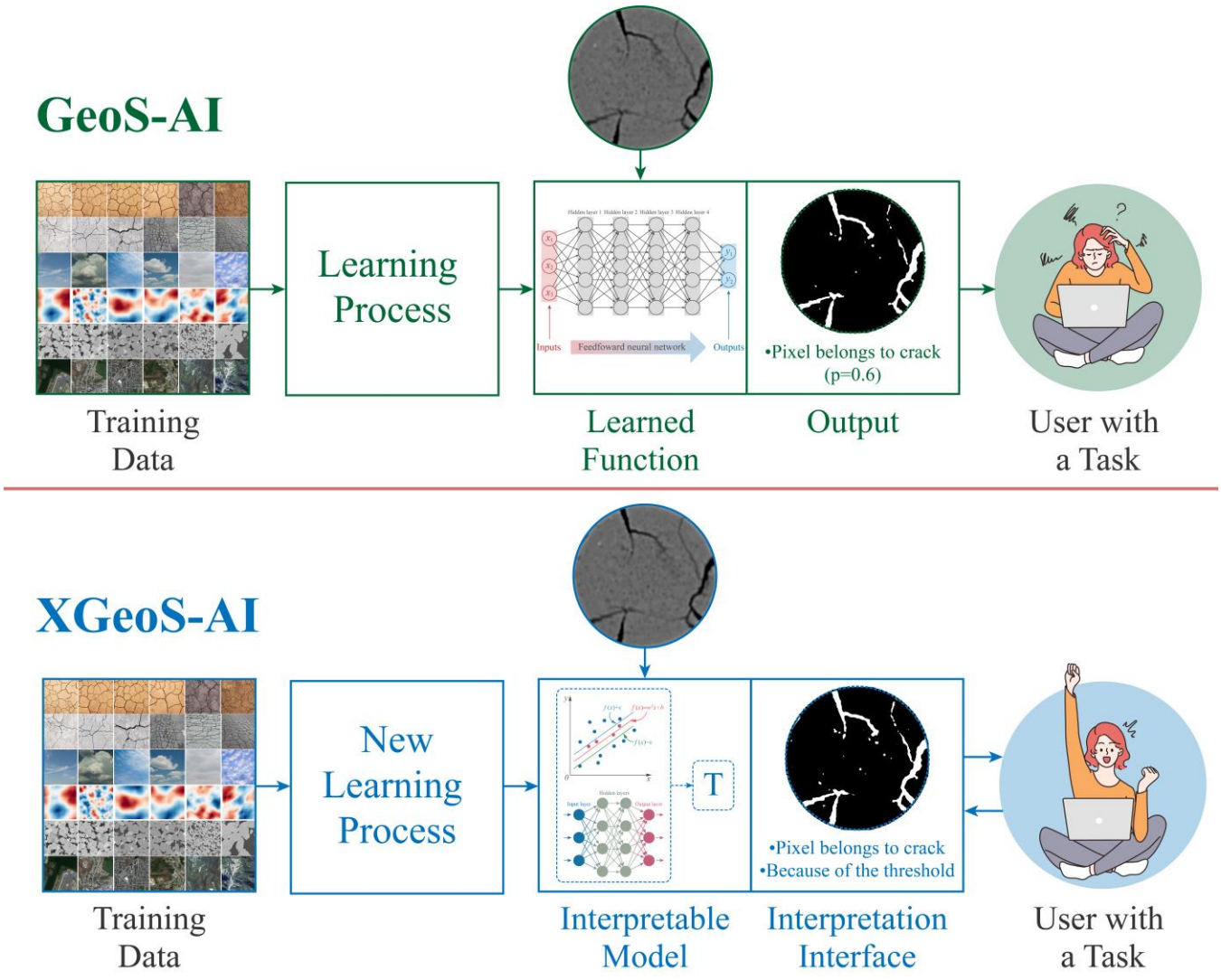

Fig 1. The comparison of conventional geoscience artificial intelligence (GeoS-AI) and interpretable geoscience artificial intelligence (XGeoS-AI).

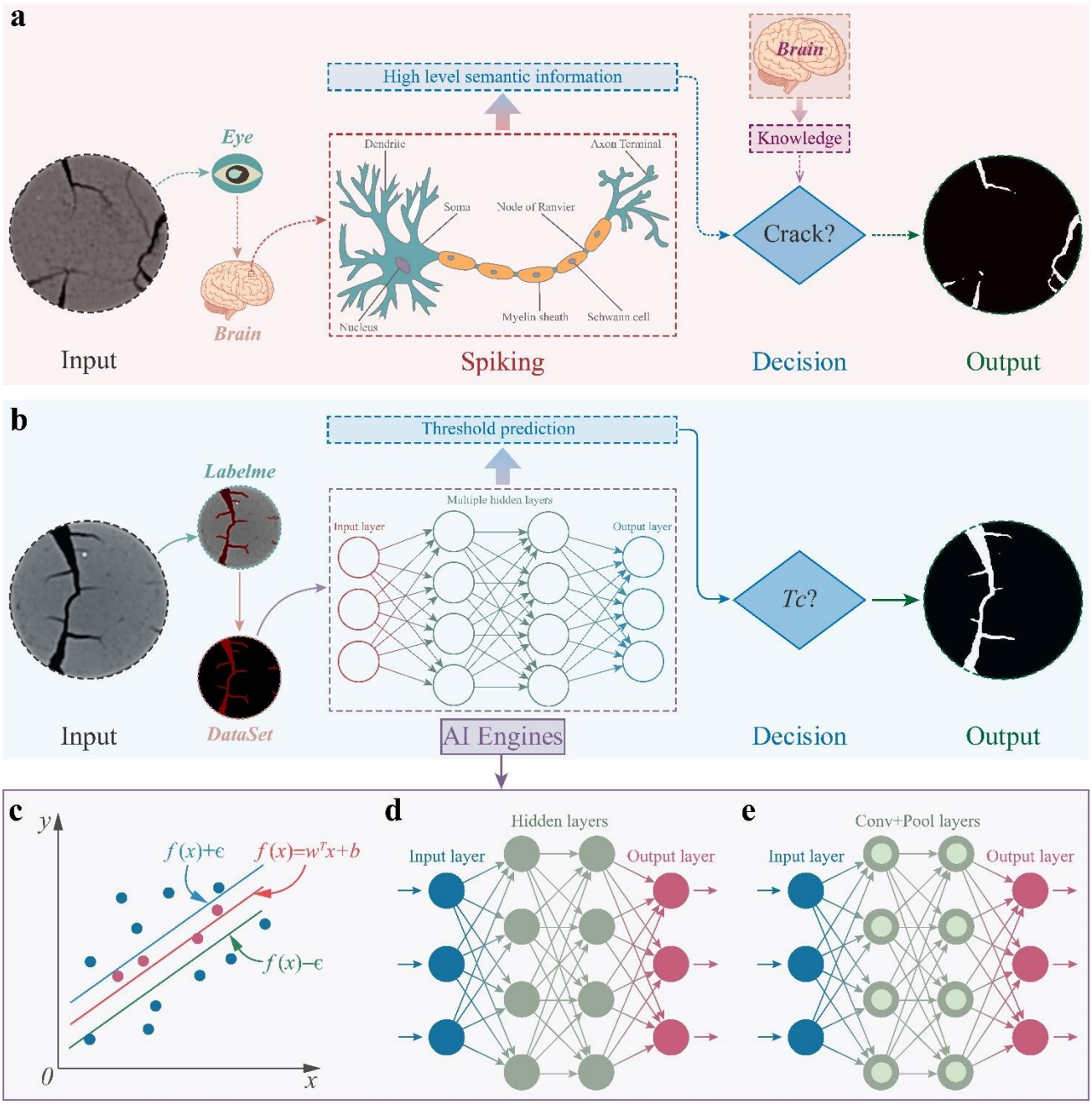

Fig 2. Interpretable geoscience artificial intelligence (XGeoS-AI) framework. (a) human-vison mechanism; (b) XGeoS-AI framework; (c)-(d) are the three typical AI engines, (c) support vector regression (SVR), (d) multilayer perceptron (MLP), (e) convolutional neural network (CNN).

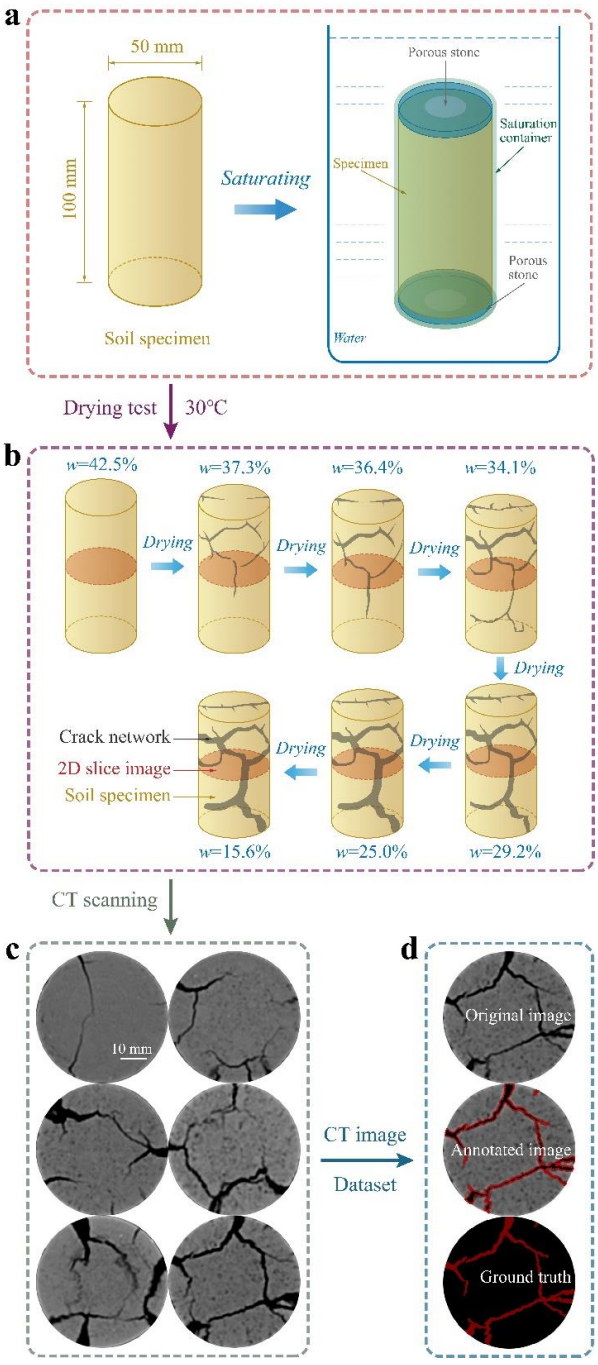

Fig 3. The process of the data preparation. (a) Soil specimen (100 mm in height and 50 mm in diameter) is placed in a saturation device under confined conditions; (b) Soil specimens with different water contents of 42.5%, 37.3%, 36.4%, 34.1%, 29.2%, 25.0%, and 15.6%; (c) CT images with different soil cracking patterns; (d) Establishment of soil crack CT image dataset.

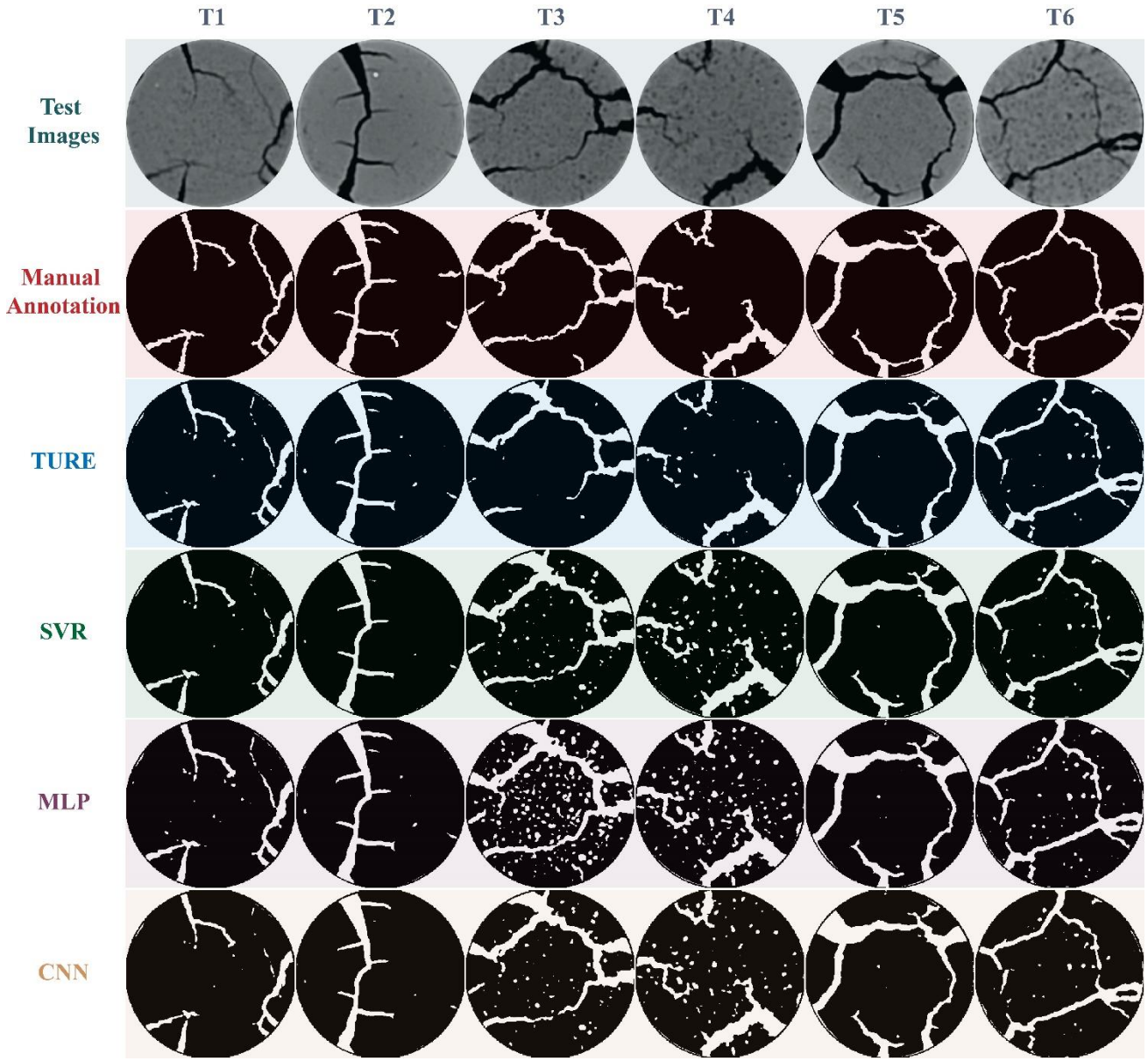

Fig 4. The visualization results of the AI engines with the proposed XGeoS-AI framework including test images, manual annotation, simple heuristic algorithm (TURE), SVR, MLP, CNN.

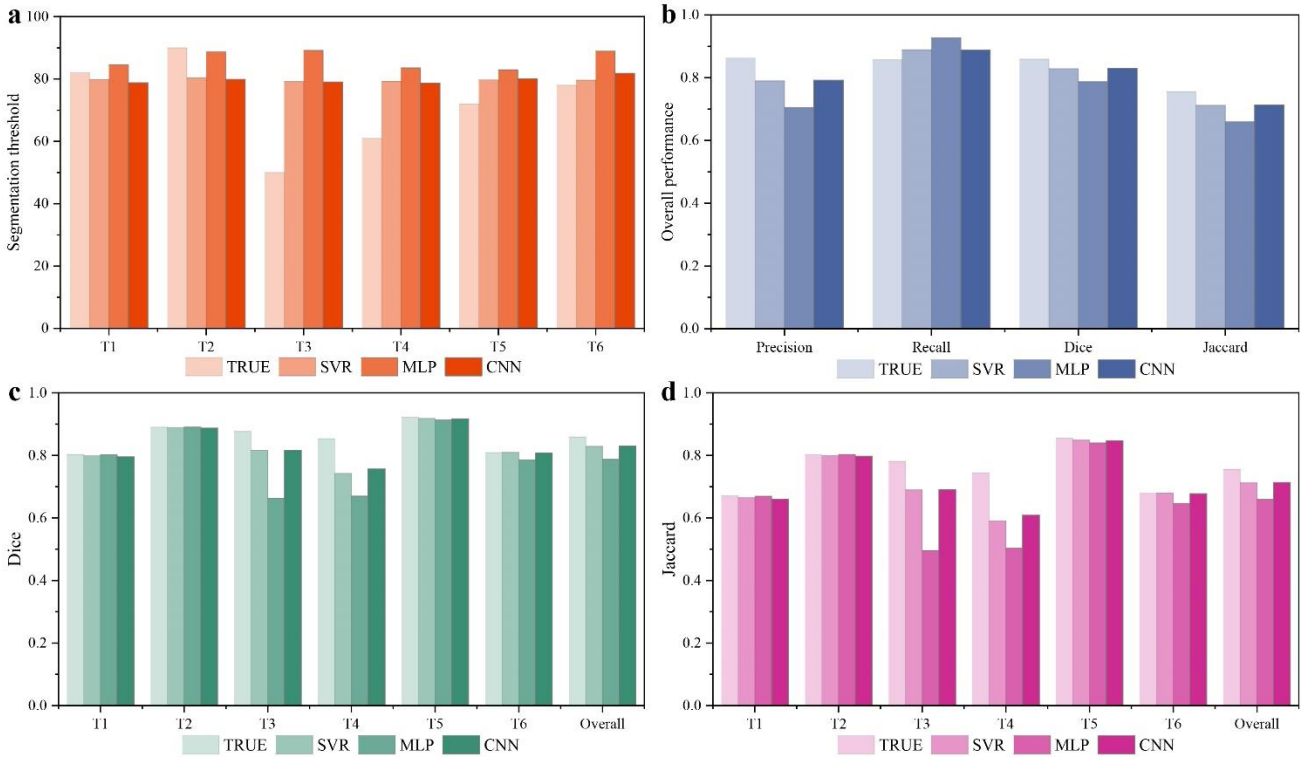

Fig 5. The numerous performance comparison of different artificial intelligence engines with the proposed XGeoS-AI framework. (a) The threshold comparison, (b) overall performance under precision, recall, dice and Jaccard, (c) dice performance, (d) Jaccard performance.

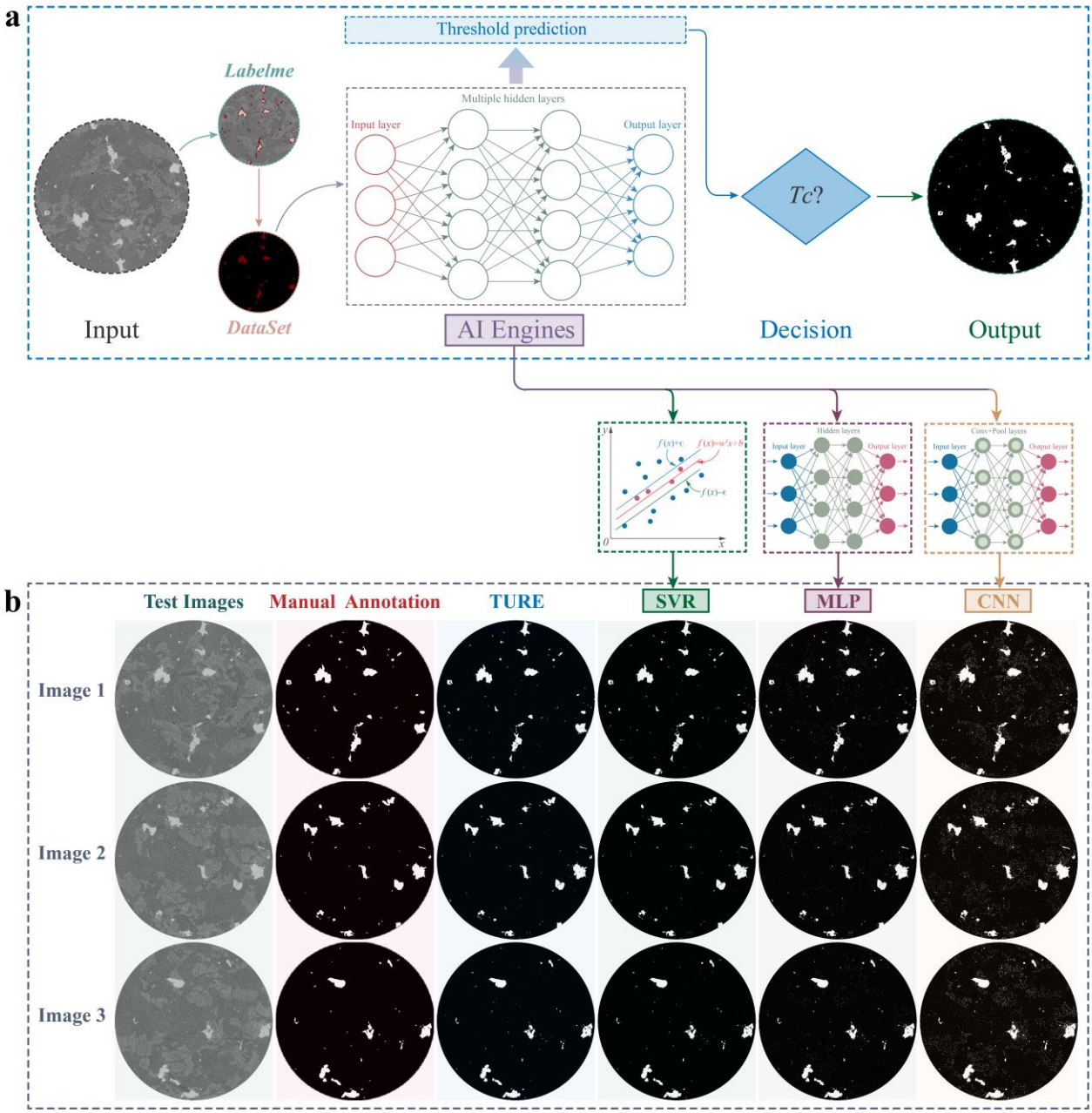

Fig 6. The proposed XGeoS-AI framework is applied in other geoscience image recognition (taking biotite distribution recognition in granite as an example). (a) The proposed framework together with three AI engines (SVR, MLP, CNN) for training and testing on the granite CT dataset; (b) Visualization results for biotite distribution recognition in granite.

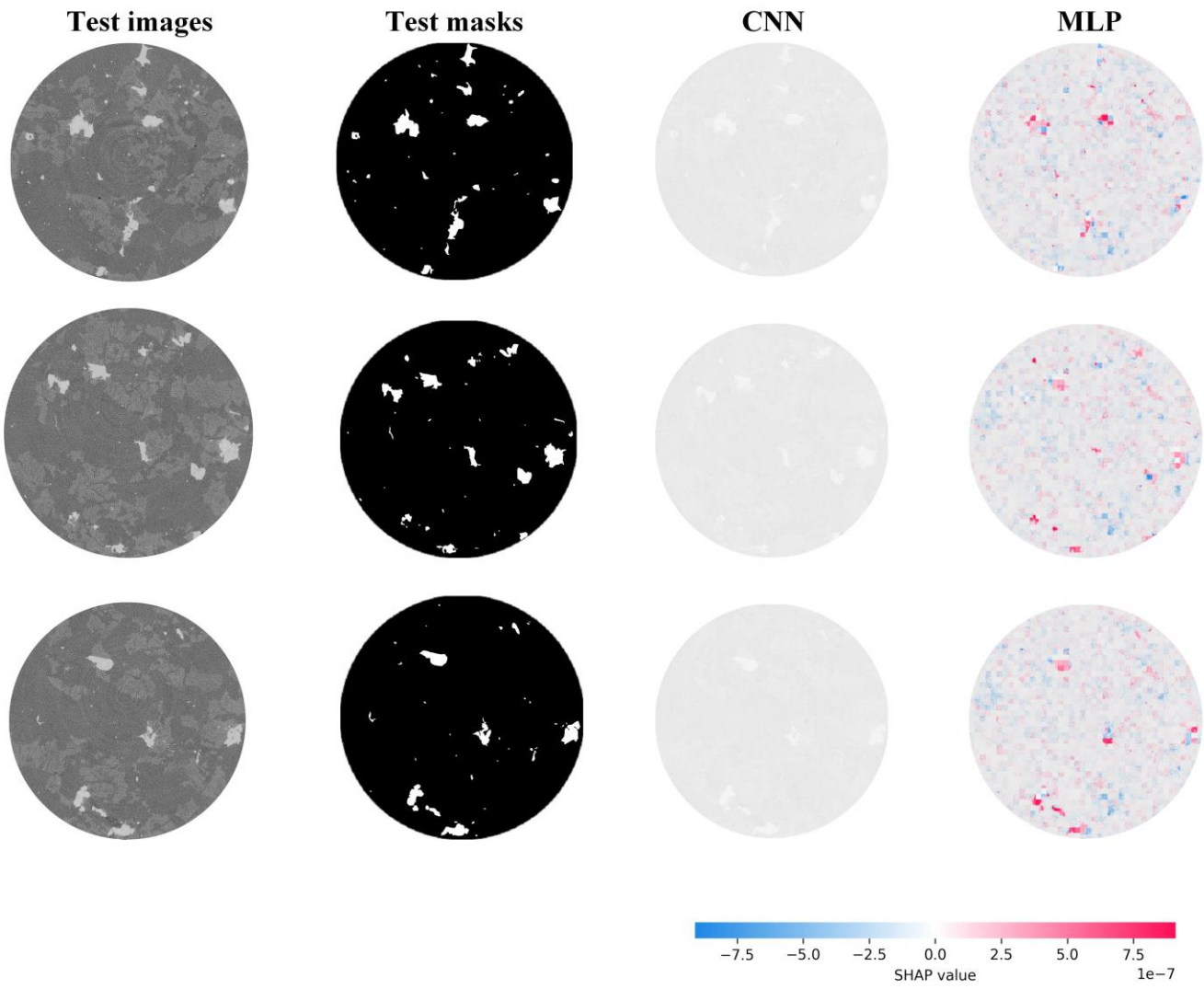

68

69 **Fig 7**. The visualization of the SHAP values for CNN and MLP engines.

70